npj | computational materials

Article

Published in partnership with the Shanghai Institute of Ceramics of the Chinese Academy of Sciences

https://doi.org/10.1038/s41524-024-01281-y

An autonomous design algorithm to experimentally realize three-dimensionally isotropic auxetic network structures without compromising density

Check for updates

Meng Shen[1,4,5], Marcos A. Reyes-Martinez[2,5], Louise Ahure Powell[2], Mark A. Iadicola[2], Abhishek Sharma[1], Fabian Byléhn[1], Nidhi Pashine[3], Edwin P. Chan[2], Christopher L. Soles[2], Heinrich M. Jaeger[3] & Juan J. de Pablo[1]

Auxetic materials have a negative Poisson's ratio and are of significant interest in applications that include impact mitigation, membrane separations and biomedical engineering. While there are numerous examples of structured materials that exhibit auxetic behavior, the examples of engineered auxetic structures is largely limited to periodic lattice structures that are limited to directional or anisotropic auxetic response. Structures that exhibit a three-dimensionally isotropic auxetic response have been, unfortunately, slow to evolve. Here we introduce an inverse design algorithm based on global node optimization to design three-dimensional auxetic metamaterial structures from disordered networks. After specifying the target Poisson's ratio for a structure, an inverse design algorithm is used to adjust the positions of all nodes in a disordered network structure until the desired mechanical response is achieved. The proposed algorithm allows independent control of shear and bulk moduli, while preserving the density and connectivity of the networks. When the angle bending stiffness in the network is kept low, it is possible to realize optimized structures with a Poisson's ratios as low as −0.6. During the optimization, the bulk modulus of these networks decreases by almost two orders of magnitude, but the shear modulus remains largely unaltered. The materials designed in this manner are fabricated by dual-material 3D-printing, and are found to exhibit the mechanical responses that were originally encoded in the computational design engine. The approach proposed here provides a materials-by-design platform that could be extended for engineering of optical, acoustic, and electrical properties, beyond the design of auxetic metamaterials.

Auxetic materials, materials with a negative Poisson's ratio, ν, contract laterally when compressed or expand laterally when stretched under uniaxial tension. This unusual mechanical response is a desirable attribute for applications such as coronary stent for medical devices[1,2], acoustic attenuation[3], impact mitigation[4,5] and seismic vibration isolation[6]. After the original discovery of re-entrant motifs in auxetic foams by Lakes and co-workers[7], the search for auxetic metamaterials has largely evolved through the gradual, Edisonian identification of auxetic motifs or the design of periodic arrangement of geometric patterns that induce auxeticity[5,8–14]. These pioneering works have revealed important design cues, such as structural re-entrancy[10], rotating squares[12] and buckling beams[14]. However, the periodic tiling of these structural elements, as in a lattice or crystalline structure, often leads to mechanical anisotropy that may not be desirable for specific engineering applications such as impact mitigation.

[1]Pritzker School of Molecular Engineering, The University of Chicago, Chicago, IL 60637, USA. [2]Materials Science and Engineering Division, National Institute of Standards and Technology, Gaithersburg, MD 20899, USA. [3]Department of Physics, The James Franck and Enrico Fermi Institutes, The University of Chicago, Chicago, IL 60637, USA. [4]Present address: Department of Physics, California State University, Fullerton, Fullerton, CA 92831, USA. [5]These authors contributed equally: Meng Shen, Marcos A. Reyes-Martinez. e-mail: depablo@uchicago.edu

Disordered structures as a starting point are advantageous in that they generally give rise to an isotropic mechanical response. The theoretical work of Goodrich et al., in particular, introduced the concept of designing disordered auxetic materials by selectively pruning local bonds that make a large contribution to the bulk modulus, B, or that have a very little effect on the shear modulus, G. Since the Poisson's ratio ν is defined as[15,16]

$$\nu = \frac{d - \frac{2G}{B}}{d(d-1) + \frac{2G}{B}}, \quad (1)$$

where d is the dimensionality, a small ν corresponds to a large ratio of G/B. Hexner et al. derived a theoretical expression to quantify the bond-level responses to bond removal in a central-force spring network[17]. Reid et al. demonstrated the effectiveness of the concept of local bond pruning by designing and successfully fabricating 2D auxetic materials. In that work, an angle bending potential energy term was included in the model, leading to good agreement between simulated designs and experimental measurements[18,19]. A material removal strategy through bond pruning was also implemented by Reyes-Martinez et al. to control the transmitted stress upon impact in three-dimensional disordered metamaterials. While effective in reducing the peak transmitted stress more efficiently than random material removal, this pruning strategy was not able to independently control bulk, B, and shear moduli, G[20]. More recent studies have implemented disorder to generate auxetic behavior in materials design. 2D auxetic metamaterials were achieved by Wang et al. through the application of disordered distribution of peanut-shaped perforations, demonstrating that order is not necessary to achieve auxetic behavior. Nevertheless, this study was limited to 2D architectures[21]. Crumpled sheets of material, such as paper, are inherently disordered and have been shown to exhibit auxetic behavior[22]. Gimenez-Ribes et al. studied the mechanisms through which auxeticity arises and showed that the compaction levels affect the shear-to-bulk modulus ratio[23]. A joint computational and experimental study demonstrated that electrospun fiber networks can display large out-of-plane expansion during uniaxial extension[24,25]. Domaschke et al. hypothesize that the large volume change is due to fiber segments undergoing out-of-plane buckling, while other fibers align with the direction of uniaxial tension.

It is helpful to point out some of the features or differences that arise in 3D versus 2D networks. Eq. (1) indicates that auxetic materials require that $\frac{G}{B} > \frac{d}{2}$. In 2D, $G > B$ is sufficient to achieve auxecticity. In 3D, this requirement increases to $G > 1.5B$ which is more difficult to realize experimentally. The local bond pruning method discussed above removes one bond at a time and, in 3D, both the bulk and shear moduli are generally reduced upon removal of the bond. There is also an additional rotational degree of freedom for each bond in 3D which does not arise in 2D; just the angle bending term employed for design of 2D networks[18] is not sufficient to properly account for the additional bond rotation in 3D[26]. In this work, we circumvent some of these challenges by designing 3D auxetic networks from disordered networks using a global node optimization strategy where the nodes are defined as the junction points where multiple bonds are joined together. Rather than prune individual bonds, in this approach we the shift spatial location of a node, re-adjust the corresponding bond lengths and angles locally required to accommodate this node displacement, and then evaluate the ramifications of this shift on the shear and bulk moduli of the network. Subsequent shifts to the global networks of nodes are optimized to achieve the designed mechanical response, akin to the pruning technique. Our computational designs are then validated by 3D printing these networks using a dual-material process, and compare the experimentally measured mechanical properties of our physical networks to the underlying predictions. We find that the combination of a model that accounts for the rotational degrees of freedom in 3D, and a global node optimization strategy, are sufficient to design 3D disordered auxetic networks whose behavior is in agreement with our experimental observations. We show that the Poisson's ratio of 3D disordered networks can be tuned to values that range from $\nu \approx 0.4$ to -0.6. The design approach adopted here has the advantages of being computationally efficient, and provides independent control of the shear modulus and the bulk modulus at any given density.

Results and discussion

Design algorithm

The starting point for our computational design strategy is a disordered network generated by the packing of frictionless spheres[27]. The simulations for jammed soft spheres were performed in LAMMPS with an overlap in soft spheres translating into a bond in a recipe similar to the one reported elsewhere[18]. Thus, the network consists of bonds connected at the junctions between the spheres that we refer to as nodes (Fig. 1a, inset). The computational model includes node-specfic bond-stretching stiffness, quantified through a constant k_b, and bond-specific angle bending stiffness, quantified by k_θ. The angle bending resistance is distributed over all possible angles a given bond can form at a given node, which for a coordination of N_c bonds leads to a total of $N_c - 1$ associated angles. Specifically, $k_\theta = \frac{(N_c-1)k'_\theta}{2}$, where N_c is the coordination number and k'_θ is the angle bending resistance between a pair of bonds connected to the same node (Fig. 2a). In this model k_θ represents the angle bending resistance on one bond resulting from all other bonds connected to the same node; the factor of 2 accounts for the rotational degrees of freedom for a bond in 3D. The constants k_b and k'_θ appear in the Hamiltonian of Eq. (5), described in the Methods section. Note that k_b, k_θ and k'_θ are all in units of energy and can be directly compared with each other. We note that the angle bending terms adopted here guarantee the conservation of angular momentum, and a similar term of k'_θ has been adopted by Rens et al.[26]. As illustrated in Fig. 1a, the global node optimization method adjusts node positions by iteratively displacing the coordinates of all nodes to increase the ratio of the shear modulus to the bulk modulus, G/B, thereby reducing the Poisson's ratio, ν (contour lines in Fig. 1a). During the optimization, the shear and bulk moduli are calculated from the elastic constants as specified in the Methods section, where additional details are provided. For simplicity, iter0 refers to the non-optimized network, and the resulting network after iterating the global optimization step # number of times is referred to as iter#. Throughout the optimization, the total number of nodes remains constant, but the bond length distribution changes with each iteration. Figure 1b, c shows the simulated bulk and shear moduli of representative networks with $k_\theta/k_b = 0.001$ as a function of the number of iterations. One can appreciate that the global node optimization approach significantly reduces B without altering G of the node-optimized mechanical metamaterial, leading to a significant reduction of B/G, and consequently, ν. Computationally, it is possible to realize a significant auxetic response ($\nu < -0.5$) after only 25 global node optimization iterations (Fig. 1d). Figure 1b–d shows results for disordered networks with two different coordination numbers, $Z = 6.1$ and $Z = 7.2$. For each coordination number, multiple different initial networks were evaluated with the resulting uncertainties reported in the Figure. This repeatability points the general effectiveness of this strategy for altering the Poisson's ratio ν to consistently low negative values (< -0.5), regardless of the initial network structure. Figure 1e, f serves to validate the proposed approach by uniaxially compressing in the vertical direction a representative network with an average coordination number $Z = 6.1$, before and after global node optimization. The global uniaxial compression of iter0 (up to a strain of $\varepsilon = -0.1$) shows that the structure behaves like a conventional material having $\nu = 0.4$. Beyond a strain of $\varepsilon = -0.1$, the bonds in the network start to touch and overlap with each other, leading to a nonlinear mechanical response. In contrast, upon uniaxial compression to $\varepsilon = -0.1$, the

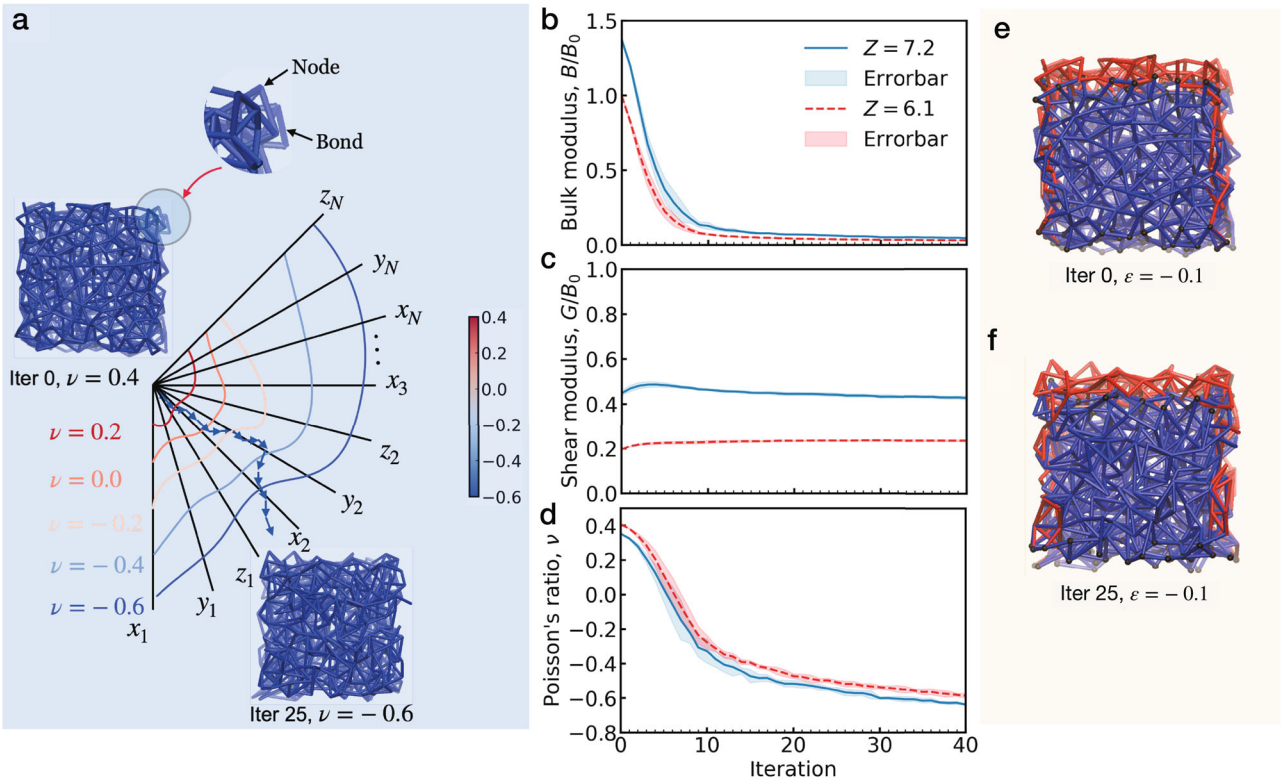

Fig. 1 | Computational results of 3D auxetic metamaterials from disordered networks by global node optimization. a Two-dimensional representation of the 3N-dimensional global node optimization, where N is the number of nodes in a network. Each initial network consists of a random arrangement of bonds and nodes (inset). The geometry of the 3D network evolves after the optimization steps. During global node optimization, the positions of all nodes, i.e., x_i, y_i and z_i, $1 \le i \le N$, are updated in each iteration step to reduce the Poisson's ratio (ν). This process is shown via a representative schematic path the iterations might take as they navigate through a simplified optimization landscape. **b**–**d** show the change in the (**b**) bulk modulus, B, (**c**) shear modulus, G, and (**d**) Poisson's ratio, ν, as a function of global node optimization iteration steps for networks of different coordination numbers of $Z = 6.1$ and $Z = 7.2$, respectively. The data of each coordination number is averaged over multiple initial networks. The error bars are the standard deviation from multiple initial networks of the same coordination number. Both the bulk and shear moduli are normalized by the bulk modulus of the initial network of $Z = 6.1$, B_0, with the coordination number $Z = 6.1$ and $Z = 7.2$, respectively. The results are validated by uniaxial compression of (**e**) the initial non-optimized network (iter0) and (**f**) the auxetic network after 25 optimization steps (iter25). Clear differences in the lateral deformation are observed between the initial and the optimized network. **e** Compressing in the vertical direction a network iter0 with a coordination number $Z = 6.1$ (red bonds and nodes are at 0 strain as references) to a strain of $\varepsilon = -0.1$ (blue bonds and nodes), we find that $\nu = 0.4$. **f** Compressing iter25 to the same strain results in $\nu = -0.3$.

optimized network is predicted to become auxetic, with $\nu = -0.3$. In addition to auxeticity, the global node optimization method produces a nearly isotropic global response from disordered networks. An example elastic stiffness matrix of a node-optimized disordered network is included in Supplementary Note 6.

As shown in Fig. 1d, Poisson's ratio is predicted to reach a value of −0.6 after approximately 40 optimization steps. That value is comparable to the experimental value of $\nu = -0.7$ reported for the first auxetic foam[7].

Angle bending stiffness

Recent work indicates that the tunability of auxetic behavior becomes limited when the ratio of angle bending stiffness, k_θ, to the bond stretching stiffness, k_b, increases towards unity[18] (as indicated earlier, k_θ and k_b and the corresponding energy terms are defined in detail in the Methods section.)

To further explore the regime of angle bending stiffness where global node optimization is effective, we vary the stiffness constant over three orders of magnitude, $k_\theta/k_b = 0.001$, 0.01 and 0.1, and investigate the extent of tunability of the moduli and Poisson's ratio. The effects of k_θ/k_b on the changes in ν, B and G for a $Z = 6.1$ network are shown in Fig. 2b–d, respectively. The simulation results in Fig. 2b indicate that the optimization algorithm is effective at reducing ν of the resulting metamaterials when k_θ is two or three orders of magnitude smaller than k_b. We find that ν continues to decrease after every iteration until it reaches values as low as ≈−0.7 after 30 optimization steps for $k_\theta/k_b = 0.001$. Although the initial value of ν is lower for the $k_\theta/k_b = 0.1$ system when compared to the cases of $k_\theta/k_b = 0.001$, 0.01, it appears that ν does not decrease significantly even after 30 global node optimization iterations for $k_\theta/k_b = 0.1$, which is qualitatively consistent with observations by Pashine et al.[28]. To gain a deeper understanding of the effect of angle bending stiffness on optimization efficiency, we decompose B and G into contributions from k_b and k_θ. Figure 2c shows that k_θ does not directly contribute to B, regardless of the magnitude of k_θ/k_b, which is consistent with the definition of B in terms of the stress and strain tensor[15] and the fact that the trace of the stress tensor is not influenced by k_θ. The stress tensor is always tangential to the bond it acts on[29]. Although k_θ does not directly contribute to the bulk modulus, B, k_θ indirectly affects the evolving value of B during optimization, i.e., the higher the k_θ, the higher is the plateau value of B after optimization, which could be attributed to the non-affine nature of the deformations in disordered networks[30,31]. A higher plateau for B inhibits further reduction of ν for $k_\theta/k_b = 0.1$, compared with the other two cases for smaller k_θ, which have a higher shear modulus (and lower Poisson's ratio) for the initial network (with $k_\theta/k_b = 0.1$) compared with initial networks with lower k_θ/k_b values.

Experimental realization

To validate our computational design method, the node-optimized mechanical metamaterial structures were converted to 3D-printer files and experimentally realized using UV-curable resins (Fig. 3). Initially, we found that the optimized mechanical metamaterials printed from a single

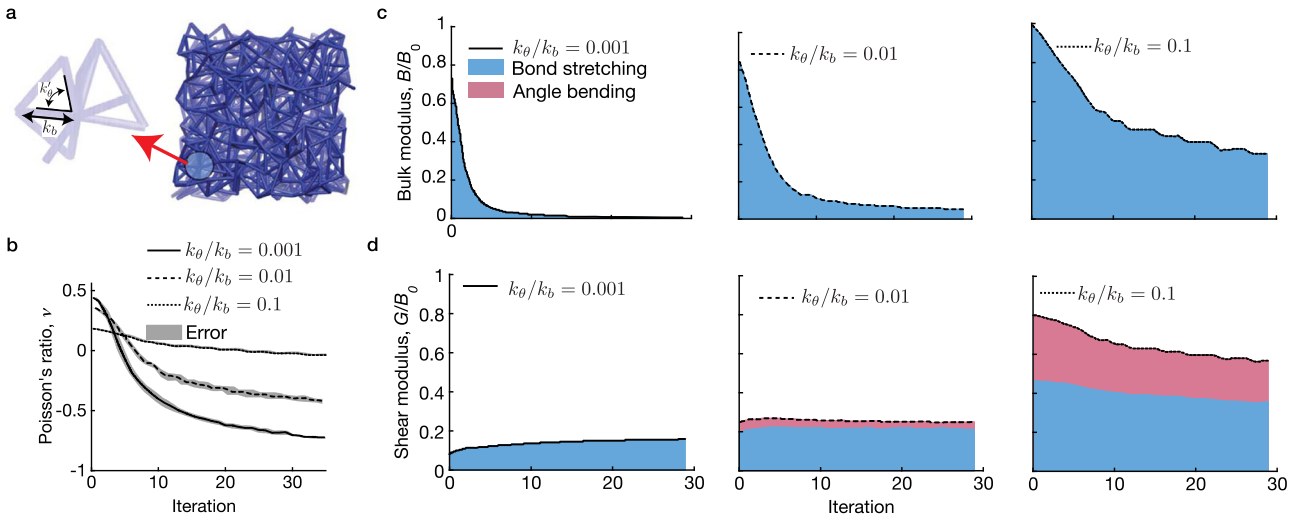

Fig. 2 | The ratio of angle bending stiffness, k_θ, to the bond stretching stiffness, k_b. **a** Definition of k'_θ and k_b in a network. The angle bending stiffness, $k_\theta = \frac{(N_c-1)k'_\theta}{2}$, represents the accumulated effect of k'_θ's associated with each bond, where N_c is the coordination number. The factor of 2 corresponds to the rotational degrees of freedom for a bond in 3D. **b** Reduction of Poisson's ratio as a function of iteration steps for different local stiffness ratios: $k_\theta/k_b = 0.001$, 0.01, and 0.1. In the regime of $k_\theta/k_b \leq 0.1$ explored here, the lower limit of the Poisson's ratio increases with k_θ/k_b. The error bars are the standard deviation from multiple initial networks of the same coordination number. **c** Bulk modulus vs. global node optimization iteration steps for $k_\theta/k_b = 0.001$, 0.01, and 0.1. Only the bond-stretching stiffness directly contributes to the bulk modulus, B. **d** Shear modulus vs. global node optimization iteration steps for $k_\theta/k_b = 0.001$, 0.01, and 0.1. The change in G during optimization is strongly dependent on the ratio between the angle bending stiffness and the bond-stretching stiffness, k_θ/k_b. The moduli are both normalized by B_0, the reference bulk modulus of the un-optimized networks when $k_\theta/k_b = 0.1$.

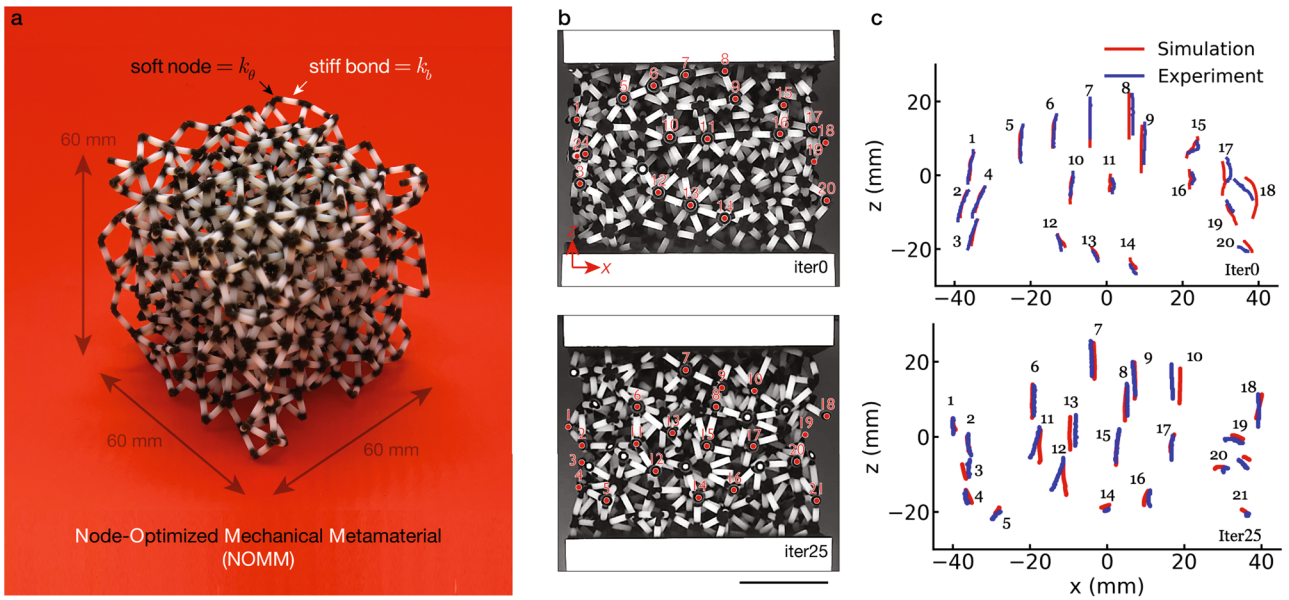

Fig. 3 | Experimental realization and comparison with simulations of the deformation behavior of node-optimized mechanical metamaterials. **a** Representative node-optimized mechanical metamaterial sample fabricated via 3D-printing. The experimental control of k_θ/k_b is achieved via dual-material 3D-printing (Methods section), where the nodes are printed with a soft elastomeric resin while the bonds are printed with a relatively stiffer resin. **b** Images of the uniaxially compressed iter0 and iter25 samples. The numbered points correspond to front-facing nodes that are tracked during compression up to $\varepsilon = -0.1$. Scale bar is 20 mm. **c** Trajectories of the tracked points for the iter0 and iter25 samples. A comparison of the experimental and simulation results of the tracked points shows that the simulated point displacements are in close agreements with experiments in the regime of small strains ($-0.01 \leq \varepsilon \leq 0$). In this limit, the measured Poisson's ratio for iter0 is $\nu = 0.37 \pm 0.03$, while iter25 exhibits $\nu = -0.24 \pm 0.05$.

homogeneous constituent material (with constant bond thickness) did not exhibit an auxetic response. This is because networks with homogeneous and uniformly thick bonds do not satisfy the condition of $k_\theta \ll k_b$ that was identified by our computational models. To reduce the angle bending resistance of the nodes while maximizing the stretching resistance of the bonds, we developed a dual-material 3D printing strategy. Specifically, we printed the nodes from a soft elastomeric polymer and chose a stiffer polymer as the material for bonds (Fig. 3a) (see Methods section). This dual-material printing strategy permits adjusting the magnitude of k_θ by simply changing the relative stiffness of the two materials. Although not systematically investigated here, we have also studied the shape of the end portion of the bonds to control k_θ (Supplementary Fig. 2). For the mechanical tests presented here, the choice of dual-material composition and bond shape approach the behavior predicted for $k_\theta/k_b = 0.01$.

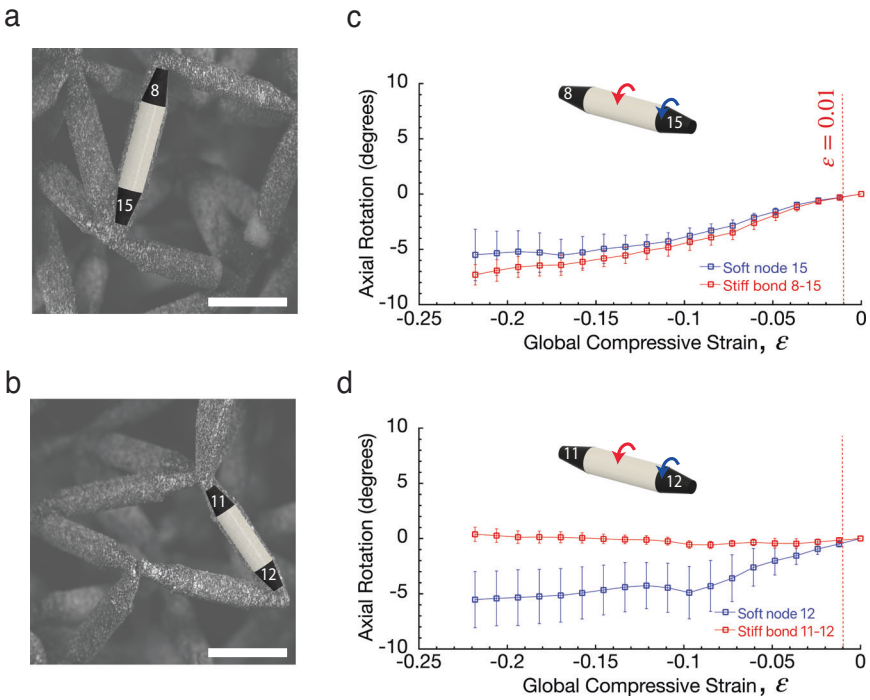

Fig. 4 | Digital Image Correlation (DIC) analysis of representative bonds and nodes. a Photograph of patterned network with highlighted region of interest along the bond connecting nodes 8 and 15. **b** Photograph of patterned network with highlighted region of interest along the bond connecting nodes 11 and 12. **c** Axial rotation with respect to soft node 8 as a function of global compressive strain. **d** Axial rotation with respect to node 11 as a function of global compressive strain. Error bars are the standard deviations of mean axial rotation along the length of the bond in both the soft and stiff regions, respectively. Scale bar represents 5 mm.

The upper and lower images in Fig. 3b represent the iter0 and iter25 samples, respectively. The colored dots on the metamaterial networks are the individual nodes that we tracked as a function of the global compressive strain ε from 0 to -0.1. As shown in the videos of the compression tests (Supplementary Video 1, adjusted 100× of the actual speed for clarity), the iter0 network expands in the lateral direction, whereas the iter25 network contracts laterally upon compression. Simulation (red curves) and optical (blue curves) tracking of the node trajectories from both samples during compression testing (Fig. 3c) show excellent agreement. For small strains, the simulation and experimental trajectories of all the nodes overlap almost perfectly. The two sets of data begin to slightly diverge at higher strains. We attribute these deviations to nonlinear effects that occur when neighboring nodes and bonds in the 3D-printed networks impinge upon each other and distort at high compressive strain. Also note that, in the interest of generality, our simulations use periodic boundary conditions, whereas the printed samples have a finite size and boundaries. Overall, the agreement between simulations and experiments is particularly encouraging, given the simplicity of the models adopted here.

We find that simulation and experimental compression measurements for iter0 exhibit $\nu \approx 0.4$ up to $\varepsilon \approx -0.1$ (Supplementary Fig. 3). Results for iter25 show that $\nu = -0.24 \pm 0.05$ at small strains, which is slightly larger than what was predicted for an infinitely large (periodic) sample (Fig. 2b). The experimentally measured ν increases with increasing compressive strain, but remains <-0.1 up to $\varepsilon = -0.1$. The effectiveness of the optimization strategy in tuning the auxetic nature of disordered networks can also be appreciated in the videos of quasi-static uniaxial compression tests (Supplementary Video 1).

Local bond strain measurements

The Hamiltonian in our model (Eq. (5)) does not take into account the axial rotations of bonds since we do not expect torsional deformations to be significant in the low strain regime ($-0.01 \le \varepsilon \le 0$). To assess if such axial bond twisting is present during the experiments, we perform Digital Image Correlation (DIC) analysis on two representative bonds with their respective nodes as labeled in Fig. 3c. This DIC analysis compares the strains in the bond between nodes 8 and 15 (Fig. 4a), as an example of where the simulated trajectory of nodes is in good agreement with experiment, with the strain in the bond between nodes 11 and 12 (Fig. 4b), as an example of where the simulated trajectory of the nodes deviate from experiment at high strains. Figure 4c confirms that significant amount of axial twist are not observed for global compressive strains between 0 and -0.01. As the global strain increases, the entire soft and stiff portions of the bond rotate in concert about the bond axis with respect to node 8 (Supplementary Video 2). Differences of less than 5° between the axial rotation of soft node 15 and the stiff portion are observed for $\varepsilon \le -0.05$. For the case of the bond between between nodes 11–12, Fig. 4d shows that there is no rotation in the stiff and soft portions of the bond for $-0.01 \le \varepsilon \le 0$ and that both portions rotate axially almost concomitantly up to $\varepsilon = -0.02$. However, as the compressive strain increases, the soft node 12 rotates, while the stiff bond stays relatively unchanged with respect to node 11; we start to see evidence of a twist loading of the bond that was not accounted for in the model. We believe that this is in part of the reason why the experiments deviate from the modeling between these nodes, especially at higher global compressive strains. The rate of increase in axial rotation changes in soft node 12 after $\varepsilon \approx -0.085$ due to member contact with a another bond connected to node 12 (Supplementary Video 3). This contact causes a directional shift in the axial rotation, which is again, not allowed in the model. In both cases, we observe that the nodes with higher coordination numbers are able to rotate together with the stiff portion of the bond, while the node in the same bond with lower coordination experiences the most relative rotations. Additional DIC data is included in Supplementary Note 4. Since relatively small axial rotation is observed in both examples, we conclude that axial rotations do not contribute significantly to the overall deformation energy of the network and hypothesize that the differences in node trajectory are mainly due to member contacts that develop as a function of compression, especially at high compressive strains. Further analysis of the necessity of torsional constraints in simulations is included in Supplementary Note 5.

Decoupling shear and bulk moduli

Poisson's ratio in most material systems, and thus the ratio of B/G, generally correlates with the packing density of the structural units[16]. This correlation is evident in plots of B/G versus density, ρ, across a wide spectrum of materials as illustrated in Fig. 5a. This correlation is more clearly observed for aluminum foams and porous silicon nitride, where the reduction in ρ is accompanied by an almost linear decrease in B/G across a density range from 0.43 to 1.39 g cm^{-3}, and a range from 2.12 to 3.28 g cm^{-3},

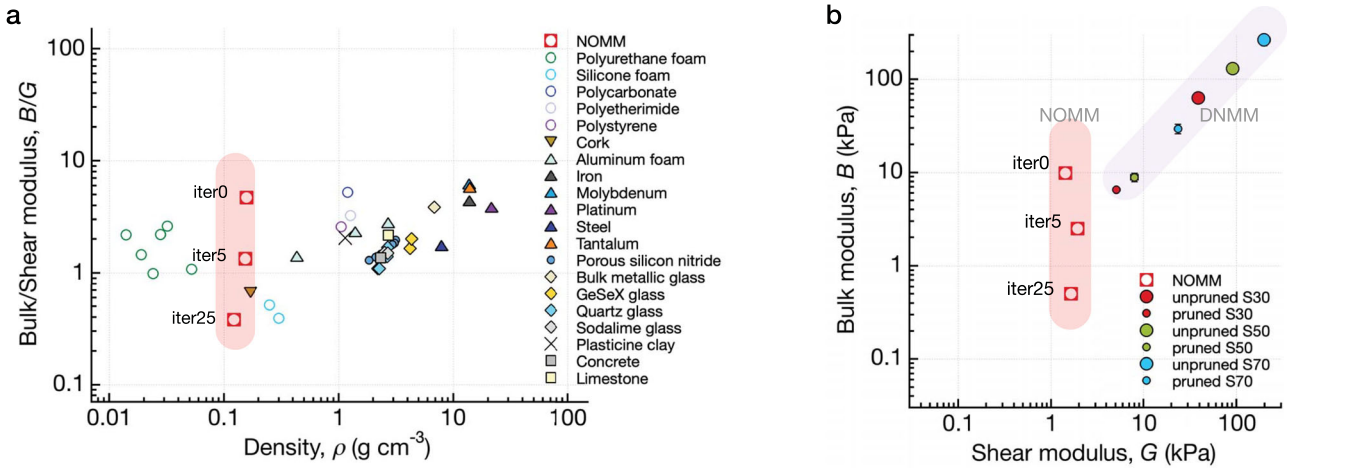

Fig. 5 | Comparison of material properties of node-optimized mechanical metamaterials with conventional engineering materials. a Ratio of bulk to shear modulus (B/G) vs. mass density (ρ) for a variety of materials[32,33,40–51]. The results for the node-optimized mechanical metamaterials show that the change in B/G is independent of ρ. **b** A plot of B vs. G illustrates the decoupling between shear and bulk moduli for the node-optimized mechanical metamaterials compared to three-dimensional disordered network mechanical metamaterials (DNMM) obtained through pruning strategy previously published[20].

respectively[32,33]. The results for our 3D-printed node-optimized mechanical metamaterials are also included in Fig. 5a, illustrating a notably different trend. In our 3D-printed metamaterials, the density appears to be decoupled from the elastic moduli; we can generate a ten-fold reduction of B/G at a constant density when we transition from iter 25 to iter 0. Figure 5b shows that for the optimized metamaterials, the bulk modulus varies over an order of magnitude, while the shear modulus is almost unchanged, leading to significant changes in ν (as predicted by Eq. (1)). Based on the results of our calculations, we anticipate that further reductions in ν could be realized with improvements to our dual-material printing process and printing material selection.

It is also helpful to point out that the global node optimization methodology developed here enables independent control of B and G. Figure 1b, c show that one can reduce B while keeping G constant. It is also possible to vary G while holding B constant using the same approach. Independent control of B and G by pruning disordered two-dimensional networks has been demonstrated by Goodrich et al.[15]. However, our attempts to implement the pruning approach to realize three-dimensional disordered networks have met with limited success (Supplementary Fig. 1). Figure 5b shows that both B and G decrease during bond pruning, as illustrated by the disordered network metamaterial (DNMM) data that was recently reported elsewhere[20]. As mentioned earlier, this is due to the more challenging requirement that $G > 1.5B$ in 3D, the non-trivial correlation between the local bond contribution to the bulk and shear moduli[15,18], and the contribution of torsional deformations to the mechanical properties. Removing a bond generally leads to a reduction of the shear modulus; in the work of Goodrich et al. one sees that only 2% of the bonds need to be removed to reach auxecticity. However in the work of Reid et al.[18], for an initial network with a coordination number of 4 (a threshold value in a 2D central force network), approximately 19% of bonds are pruned for a random network to become auxetic, and there is a danger of rendering the networks under-coordinated. As an aside, we note that torsion terms are neglected in the model adopted here; we find that for sufficiently coordinated networks, the rotational resistance terms between pairs of bonds associated with k'_θ introduces a torsional resistance. The critical coordination number can be reduced if angle bending terms are introduced[31], and it could be further decreased by incorporating explicit torsional terms.

The simulation results suggest that further reductions in ν could be realized through improvements to the dual-material printing process and through alternative choices for the printing materials. It is possible that limitations in the mapping of simulations to experiments can be improved by printing material choices. Moreover, the design method as implemented here is limited to relatively small strains. Future research could improve the prediction and design of mechanical responses into the nonlinear region by refining the computational models, e.g. by including steric interaction between bonds and torsional energy contributions, by pushing the structures to the limit of under-coordinated networks and the regime where the angle bending stiffness[26] and torsional stiffness are higher than the bond stretching stiffness.

In conclusion, the approach adopted here for design of 3D auxetic metamaterials from disordered networks leads to facile development of isotropic, highly auxetic structures. The designs conceived here on the basis of computational models have been produced in the laboratory by 3D printing, and are found to exhibit mechanical properties that are in good agreement with theoretical predictions. An interesting feature of the optimization strategy introduced here is that density and topology are preserved throughout the design process, thereby facilitating tuning of the Poisson's ratio without the loss of mechanical integrity. The level of control that is achieved by simultaneous adjustment of all node positions could be particularly useful for development of materials that exhibit multiple designer properties, including mechanical, optical, or thermal characteristics.

Methods

Certain instruments and materials are identified in this paper to adequately specify the experimental details. Such identification does not imply a recommendation by the National Institute of Standards and Technology, nor does it imply that the materials are necessarily the best available for the purpose.

Bond pruning

In the bond-pruning method, every pruning step proceeds as follows: 1. A bond i is tentatively removed from the network, where i is the bond index. Then the decrease in B, G and ν, namely ΔB_i, ΔG_i and $\Delta\nu_i$ are calculated for the network. The tentatively removed bond is then put back to the network. We repeat this procedure for every bond in the network. 2. We select a bond to be permanently removed based on the pruning protocol: The bond leading to min ΔG is permanently removed.

In order to account for the redistribution of bond-level contribution to the global mechanical response after bond removal, only one bond is permanently removed at each step.

Global node optimization

The global node optimization is realized by a constrained gradient descent algorithm[34],

$$r_{i\alpha}^{n+1} = r_{i\alpha}^{n} - \lambda \frac{\partial(\nu + L_1 + L_2)}{\partial r_{i\alpha}} \tag{2}$$

where $r_{i\alpha}$ is the α component of the coordinate of node i, n is the iteration number, λ is the learning rate, and L_1 and L_2 are two constraints implemented to avoid bond overlapping and node overlapping, where

$$L_1 = l_1 \sum_j [H(\theta_{min} - \theta_j)(\theta_j - \theta_{min})]^6 \tag{3}$$

where $l_1 = 0.01$ is a constant, θ is the angle between connected bonds, j is the angle index, $\theta_{min} = 15°$ is the minimum angle allowed, and $H(\theta_{min} - \theta_j)$ is the Heaviside step function.

$$L_2 = l_2 \sum_{i,j} [H(r_{min} - r_{ij})(r_{ij} - r_{min})]^2 \tag{4}$$

where $l_2 = 1000.0$ is a constant, r_{ij} is the distance between node i and node j, $r_{min} = 0.3r_0$ is the minimum distance allowed in the length unit r_0, and $H(r_{min} - r_{ij})$ is the Heaviside step function. The choice of the two constants (l_1, l_2) was made with trial and error such that no significant overlap was observed in the optimized networks upon simulation.

At every step, the coordinate of a node i, r_i, is displaced infinitesimally in the α direction, the force field parameters for the equilibrium angle and bond length are updated accordingly, and then B, G and ν are measured for the virtually displaced network. After a scan of all the nodes in all three directions by this procedure, we calculate the gradient of $(\nu + L_1 + L_2)$ with respect to the node coordinate components. Then we update the node positions according to Eq. (2). The iterations will maximize $\frac{G}{B}$, in another word, minimize ν, under constraints defined by Eqs. (3) and (4).

To simulate the experimental networks and individual node movement, we truncated the periodic networks to a finite block, and simulated progressive uniaxial strain with the top and bottom surface nodes laterally fixed. Please see Supplementary Fig. 6 and Supplementary Video 4.

Simulation models

The elastic constants c_{ijkl} are calculated by taking the derivative of the stress tensor with respect to the strain tensor components. Energy minimization is performed in Large-scale Atomic/Molecular Massively Parallel Simulator (LAMMPS)[35,36] at different states of strain to allow calculation of various athermal elastic constants. These strain tensors were calculated by minute deformations (10^{-5} length units). A force tolerance of 10^{-9} force units were used for the convergence of energy minimization. The simulation imposes exceedingly small mechanical compressions to the structure for Poisson's ratio calculations, so they are likely in the linear response regime that is agnostic of the timescale. Additionally, since the simulation measures a static property (Poisson's ratio) at zero temperature, time scale consideration are not relevant.

G and B are calculated as $G = \frac{1}{15}(3c_{yzyz} + 3c_{xzxz} + 3c_{xyxy} + c_{xxxx} + c_{yyyy} + c_{zzzz} - c_{yyzz} - c_{xxzz} - c_{xxyy})$ and $B = \frac{1}{9}(c_{xxxx} + c_{yyyy} + c_{zzzz} + 2c_{yyzz} + 2c_{xxzz} + 2c_{xxyy})$, respectively[15,37]. The Poisson's ratio is calculated using the relationship $(\nu = \frac{3(B/G)-2}{6(B/G)+2})$ during bond pruning and optimization, and measured by the displacement of edge nodes during validation.

In the athermal limit, the Hamiltonian for the simulations is written as:

$$H = U = \frac{1}{2}\sum_i k_{bi}\frac{(l_{bi} - l_{b0i})^2}{l_{b0i}^2} + \frac{1}{2}\sum_m k'_{\theta m}(\theta_m - \theta_{0m})^2 \tag{5}$$

where U is the potential energy, k_b and k'_θ are the bond stretching resistance and angle bending resistance, respectively. $k'_\theta = \frac{2k_\theta}{N_c - 1}$, where k_θ is the total angle bending stiffness per bond with respect to each node, and N_c is the coordination number. The factor of 2 accounts for 2 rotational degrees of freedom for angle bending of each bond in 3D by a mean field approximation, as opposed to only 1 rotational degree of freedom in 2D. l_{bi} and θ_m are the bond length of bond i and the bending angle of angle m, respectively. l_{b0} and θ_0 are the equilibrium bond length and the bending angle, respectively. The bending angle is defined between two connected bonds, similar to the respective definitions in widely used classical molecular dynamics force fields[38,39]. l_{b0} and θ_0 are the equilibrium bond length and bending angle, respectively. k_b and k_θ have the same energy units and can be directly compared with each other.

Dual-material 3D-printing

To create a 3D printable model of the node-optimized mechanical metamaterials studied, we use a python script that creates one bond at a time and merges them together to form the network. Each bond of the network is considered to be a cylinder with its diameter ≈ 0.2 times the average length of the bonds. We convert this structure to an .STL file format that can then be 3D-printed.

All the node-optimized mechanical metamaterials were 3D-printed using UV-curable printing resins on a Stratasys Connex350 3D printer (Stratasys Ltd.). To minimize k_θ in the samples, the nodes were printed using materials that was significantly softer than the bond material. The stiff VeroWhitePlus (RGD835) was used as the material for the bonds and TangoBlack Plus (FLX980) as the elastomeric build material for the nodes. Mechanical properties of printing materials can be found in the Stratasys Digital Material Data sheet.

To homogenize axial compression, and to get accurate measurements of global uniaxial strain during experiments, flat plates were added to the top and bottom surfaces of all the generated networks before 3D printing (See Supplementary Fig. 7 for experimental setup and added flat plates). The top and bottom plates were printed using the elastomeric build material, TangoBlack Plus (FLX980). These flat surfaces embed the corresponding surface nodes and, consequently, limit their lateral mobility. To mimic the constrained lateral motion that the added plates impose, we performed Global Node Optimization applying constraints to the lateral motion of the surface nodes. Deep auxetic behavior was still achieved after optimization (Supplementary Video 4).

Measurement of mechanical properties

Quasi-static, uniaxial compression experiments were performed on 3D-printed node-optimized mechanical metamaterials using a Stable Microsystems Texture Analyzer TA.XTplus. Experiments were displacement-controlled at a rate of 0.1 mm s^{-1} for both loading and unloading. Force and displacement were recorded and a minimum of 3 tests were performed on each sample. A digital camera (JAI BM-500GE) captured images of the sample deformation during the experiments at a rate of 10 frames per second. Dot stickers were used on front-facing nodes to facilitate tracking of independent node movement during deformation. Node tracking analysis was performed using the Manual Tracking plugin from the open source image processing software FIJI.

The transverse strain (ε_{trans}) during deformation experiments was determined from measured sample width change. Sample width as a function of strain was measured by analyzing the recorded image sequences during deformation experiments using a custom-designed LabVIEW edge detention software routine to obtain the average sample width. Poisson's ratio (ν) was then calculated from $\nu = -\Delta\varepsilon_{trans}/\Delta\varepsilon_{axial}$. The Young's modulus ($E$) was determined from the linear section of the load-displacement curves obtained from compression experiments. Bulk modulus was determined from the measured E and ν values using the relation $B = E/3(1 - 2\nu)$. The shear modulus (μ) was determined from the linear portions of the load-displacement curves obtained from shear deformation experiments. Shear deformation experiments were performed by mounting the samples in a shear configuration and applying uniaxial shear

deformation using a Stable Microsystems Texture Analyzer TA.XTplus. Experiments were displacement-controlled at a rate of 0.1 mm s^{-1}.

Digital Image Correlation (DIC)

Samples were prepared for DIC by patterning the surface of the networks with airbrushed black and white speckles/Airbrush nozzle size: 0.6 mm. Approximate Pattern Feature Size of 85 µm. Quasi-static, uniaxial compression of disordered networks was performed using an Instron 4465 test frame with a 5kN load cell capacity. Two Point Gray 12MP - GS3-U3-123S6M cameras with F11 numerical aperture, and an exposure of 18 ms were used for stereoscopic image acquisition of the experiment. A Correlated Solutions, inc LED light with linear polarizer filters provided illumination of the specimen. The images capture a field of view of 18.18 mm × 24.82 mm at a resolution 3000 pixels × 4096 pixels (165 pixels/mm). The DIC analysis was performed using the software Vic-3D Version 8.4.0, build 626. The subset size was 91 pixels × 91 pixels with a step size of 30 pixel. The subset Shape unction was affine and a Correlation Criterion Normalized sum of squared differences (NSSD). A Hencky strain type was adopted. Strain-Filter Size Diameter: 5. Each image aquisition rate was manual (1 image/min).

Data availability

Data available upon request.

Code availability

Code available upon request.

Received: 8 December 2023; Accepted: 19 April 2024;
Published online: 29 May 2024

References

1. Evans, K. E. & Alderson, A. Auxetic Materials: Functional Materials and Structures from Lateral Thinking! *Adv. Mater.* **12**, 617–628 (2000).
2. Amin, F. et al. Auxetic coronary stent endoprosthesis: Fabrication and structural analysis. *J. Appl. Biomater. Functional Mater.* **13**, 127–135 (2015).
3. Liu, X., Hu, G., Sun, C. & Huang, G. Wave propagation characterization and design of two-dimensional elastic chiral metacomposite. *J. Sound Vib.* **330**, 2536–2553 (2011).
4. Sanami, M., Ravirala, N., Alderson, K. & Alderson, A. Auxetic Materials for Sports Applications. *Procedia Eng.* **72**, 453–458 (2014).
5. Li, D., Bu, X., Xu, Z., Luo, Y. & Bai, H. Bioinspired Multifunctional Cellular Plastics with a Negative Poisson's Ratio for High-Energy Dissipation. *Adv. Mater.* **32**, in press (2020).
6. Brûlé, S., Enoch, S. & Guenneau, S. Emergence of seismic metamaterials: Current state and future perspectives. *Phys. Lett. A* **384**, 126034 (2020).
7. Lakes, R. Foam Structures with a Negative Poisson's Ratio. *Science* **235**, 1038–1040 (1987).
8. Gibson, L. J. & Ashby, M. F. The Mechanics of Three-Dimensional Cellular Materials. *Proc. R. Soc. A* **382**, 43–59 (1982).
9. Masters, I. G. & Evans, K. E. Models for the elastic deformation of honeycombs. *Compos. Struct.* **35**, 403–422 (1996).
10. Grima, J. N. & Evans, K. E. Auxetic behavior from rotating squares. *J. Mater. Sci. Lett.* **19**, 1563–1565 (2000).
11. Grima, J. N. *New auxetic materials*. Ph.D. thesis, Exeter Univ. (United Kingdom) (2000).
12. Alderson, A. & Evans, K. E. Rotation and dilation deformation mechanisms for auxetic behaviour in the α-cristobalite tetrahedral framework structure. *Phys. Chem. Miner.* **28**, 711–718 (2001).
13. Spadoni, A. & Ruzzene, M. Elasto-static micropolar behavior of a chiral auxetic lattice. *J. Mech. Phys. Solids.* **60**, 156–171 (2012).
14. Gibson, L. J., Ashby, M. F., Schajer, G. S. & Robertson, C. I. The Mechanics of Two-Dimensional Cellular Materials. *Proc. R. Soc. A* **382**, 25–42 (1982).
15. Goodrich, C. P., Liu, A. J. & Nagel, S. R. The Principle of Independent Bond-Level Response: Tuning by Pruning to Exploit Disorder for Global Behavior. *Phys. Rev. Lett.* **114**, 225501 (2015).
16. Greaves, G. N., Greer, A. L., Lakes, R. S. & Rouxel, T. Poisson's ratio and modern materials. *Nat. Mater.* **10**, 823–837 (2011).
17. Hexner, D., Liu, A. J. & Nagel, S. R. Linking microscopic and macroscopic response in disordered solids. *Phys. Rev. E* **97**, 063001 (2018).
18. Reid, D. R. et al. Auxetic metamaterials from disordered networks. *Proc. Natl. Acad. Sci. USA* **115**, E1384–E1390 (2018).
19. Reid, D. R., Pashine, N., Bowen, A. S., Nagel, S. R. & Pablo, J. J. D. Ideal isotropic auxetic networks from random networks. *Soft Matter* **15**, 8084–8091 (2019).
20. Reyes-Martinez, M. A. et al. Tuning the mechanical impedance of disordered networks for impact mitigation. *Soft Matter* **18**, 2039–2045 (2022).
21. Wang, H., Xiao, S. & Wang, J. Disordered auxetic metamaterials architected by random peanut-shaped perturbations. *Mater. Des.* **212**, 110291 (2021).
22. Giménez-Ribes, G., Motaghian, M., van der Linden, E. & Habibi, M. Crumpled structures as robust disordered mechanical metamaterials. *Mater. Des.* **232**, 112159 (2023).
23. Giménez-Ribes, G., Van Der Linden, E. & Habibi, M. Auxetic behavior and unusual shear resistance of crumpled materials: Opportunities for programming the nonlinear responses of crumpled mechanical metamaterials. *Mater. Des.* **223**, 111258 (2022).
24. Domaschke, S., Morel, A., Fortunato, G. & Ehret, A. E. Random auxetics from buckling fibre networks. *Nat. Commun.* **10**, 4863 (2019).
25. Domaschke, S., Zündel, M., Mazza, E. & Ehret, A. E. A 3D computational model of electrospun networks and its application to inform a reduced modelling approach. *Int. J. Solids Struct.* **158**, 76–89 (2019).
26. Rens, R. & Lerner, E. Rigidity and auxeticity transitions in networks with strong bond-bending interactions. *Eur. Phys. J. E* **42**, 114 (2019).
27. Liu, A. J. & Nagel, S. R. The jamming transition and the marginally jammed solid. *Annu. Rev. Condens. Matter Phys.* **1**, 347–369 (2010).
28. Pashine, N., Reid, D. R., Shen, M., de Pablo, J. J. & Nagel, S. R. Poisson's ratio and angle bending in spring networks. Preprint at https://arxiv.org/abs/2104.03198 (2021).
29. Bekker, H. & Ahlström, P. The Virial of Angle Dependent Potentials in Molecular Dynamics Simulations. *Mol. Simul.* **13**, 367–374 (1994).
30. Head, D. A., Levine, A. J. & MacKintosh, F. Deformation of cross-linked semiflexible polymer networks. *Phys. Rev. Lett.* **91**, 108102 (2003).
31. Broedersz, C. P., Mao, X., Lubensky, T. C. & MacKintosh, F. C. Criticality and isostaticity in fibre networks. *Nat. Phys.* **7**, 983–988 (2011).
32. Kováčik, J., Marsavina, L. & Linul, E. Poisson's Ratio of Closed-Cell Aluminium Foams. *Materials* **11**, 1904 (2018).
33. Díaz, A., Hampshire, S., Yang, J.-F., Ohji, T. & Kanzaki, S. Comparison of Mechanical Properties of Silicon Nitrides with Controlled Porosities Produced by Different Fabrication Routes. *J. Am. Ceram. Soc.* **88**, 698–706 (2005).
34. Bertsekas, D. P. *Constrained Optimization and Lagrange Multiplier Methods* (Academic Press, 2014).
35. Plimpton, S. Fast parallel algorithms for short-range molecular dynamics. *J. Comput. Phys.* **117**, 1–19 (1995).
36. Thompson, A. P., Plimpton, S. J. & Mattson, W. General formulation of pressure and stress tensor for arbitrary many-body interaction potentials under periodic boundary conditions. *J. Chem. Phys.* **131**, 154107 (2009).
37. Gale, J. D. & Rohl, A. L. The General Utility Lattice Program (GULP). *Mol. Simul.* **29**, 291–341 (2003).

38. MacKerell, A. D. et al. All-Atom Empirical Potential for Molecular Modeling and Dynamics Studies of Proteins. *J. Phys. Chem. B* **102**, 3586–3616 (1998).
39. Cornell, W. D. et al. A Second Generation Force Field for the Simulation of Proteins, Nucleic Acids, and Organic Molecules. *J. Am. Chem. Soc.* **117**, 5179–5197 (1995).
40. Gibson, L. J. *The elastic and plastic behaviour of cellular materials*. Thesis, (University of Cambridge, 1981).
41. Friis, E. A., Lakes, R. S. & Park, J. B. Negative Poisson's ratio polymeric and metallic foams. *J. Mater. Sci.* **23**, 4406–4414 (1988).
42. Mark, J. E. *Polymer Data Handbook*, 2nd. edn (Oxford University Press, 2009).
43. Hixson, R. S., Boness, D. A., Shaner, J. W. & Moriarty, J. A. Acoustic Velocities and Phase Transitions in Molybdenum under Strong Shock Compression. *Phys. Rev. Lett.* **62**, 637–640 (1989).
44. Rouxel, T., Ji, H., Guin, J. P., Augereau, F. & Rufflé, B. Indentation deformation mechanism in glass: Densification versus shear flow. *J. Appl. Phys.* **107**, 094903 (2010).
45. Mohr, M. et al. Young's modulus, fracture strength, and Poisson's ratio of nanocrystalline diamond films. *J. Appl. Phys.* **116**, 124308 (2014).
46. Deschamps, T., Margueritat, J., Martinet, C., Mermet, A. & Champagnon, B. Elastic Moduli of Permanently Densified Silica Glasses. *Sci. Rep.* **4**, 7193 (2014).
47. Antao, S. M. et al. Network Rigidity in GeSe 2 Glass at High Pressure. *Phys. Rev. Lett.* **100**, 115501 (2008).
48. Ji, H., Robin, E. & Rouxel, T. Compressive creep and indentation behavior of plasticine between 103 and 353K. *Mech. Mater.* **41**, 199–209 (2009).
49. Ji, S. et al. Poisson's Ratio and Auxetic Properties of Natural Rocks. *J. Geophys. Res. Solid Earth* **123**, 1161–1185 (2018).
50. Bauccio, M. *ASM Metals Reference Book*, 3rd. edn (ASM International, 1993).
51. The Engineering Toolbox. Concrete Properties. https://www.engineeringtoolbox.com/concrete-properties-d_1223.html (2008).

Acknowledgements

The authors thank the Center for Hierarchical Materials Design (CHiMaD) for financially supporting this research. This work was partially supported by the University of Chicago Materials Research Science and Engineering Center, which is funded by the National Science Foundation under award number DMR-2011854. M.A.R. also acknowledges financial support from the National Research Council (NRC) Postdoctoral Fellowship award. This work is a contribution of NIST, an agency of the U.S. Government, and not subject to U.S. copyright. We thank Daniel Hexner for providing the packing algorithm, and Prof. Sidney Nagel for helpful discussions.

Author contributions

M.S. and M.A.R. are co-first authors. M.S. performed computational simulations of optimization, analyzed data comparing simulations and experiments and co-wrote original manuscript. M.A.R. conceived dual-material printing approach, 3D printed networks, performed quasi-static compression experiments, analyzed data and co-wrote original manuscript. L.A.P. and M.A.I., performed and analyzed DIC experiments. A.S. and F.B. performed analysis of the necessity of torsional constraints in simulations. A.S. added clarifications on the simulation details in the manuscript. N.P. provided algorithm for generation of network drawings. E.P.C. and C.L.S. provided experimental feedback and helped write original manuscript. H.M.J. provided helpful discussion, feedback and access to 3D printing facilities. J.d.P. conceived and guided the project while providing helpful discussion and feedback.

Competing interests

The authors declare no competing interests.

Additional information

Supplementary information The online version contains supplementary material available at https://doi.org/10.1038/s41524-024-01281-y.

Correspondence and requests for materials should be addressed to Juan J. de Pablo.

Reprints and permissions information is available at http://www.nature.com/reprints

Publisher's note Springer Nature remains neutral with regard to jurisdictional claims in published maps and institutional affiliations.

Open Access This article is licensed under a Creative Commons Attribution 4.0 International License, which permits use, sharing, adaptation, distribution and reproduction in any medium or format, as long as you give appropriate credit to the original author(s) and the source, provide a link to the Creative Commons licence, and indicate if changes were made. The images or other third party material in this article are included in the article's Creative Commons licence, unless indicated otherwise in a credit line to the material. If material is not included in the article's Creative Commons licence and your intended use is not permitted by statutory regulation or exceeds the permitted use, you will need to obtain permission directly from the copyright holder. To view a copy of this licence, visit http://creativecommons.org/licenses/by/4.0/.

© The Author(s) 2024